Article

Not peer-reviewed version

Novel NH4V4O10-Reduced Graphene Oxide Cathodes for Zinc-Ion Batteries: Theoretical Predictions and Experimental Validation

He Lin *, Chenfan Liu , Yu Zhang

Posted Date: 24 June 2024

doi: 10.20944/preprints202405.0122.v2

Keywords: zinc-ion batteries; cathode materials; NH4V4O10; reduced graphene oxide

 doi:10.20944/preprints202405.0122.v2

Article

Novel $NH_4V_4O_{10}$-Reduced Graphene Oxide Cathodes for Zinc-Ion Batteries: Theoretical Predictions and Experimental Validation

He Lin *, Chenfan Liu and Yu Zhang

A State Key Laboratory of Chemistry and Utilization of Carbon Based Energy Resources, School of Chemistry, Xinjiang University, Urumqi 830017, China; mackim1005@gmail.com (C.L.); cnuo017@gmail.com (Y.Z.)

* Correspondence: helin@xju.edu.cn; Tel.: +86-180-4090-9207

Abstract: This investigation explores the potential of enhancing aqueous zinc-ion batteries (AZIBs) through the introduction of a novel cathode material, $NH_4V_4O_{10}$ (NVO), combined with reduced graphene oxide (rGO). Utilizing Density Functional Theory (DFT), it was hypothesized that the incorporation of rGO would increase the interlayer spacing of NVO and diminish the charge transfer interactions, thus promoting enhanced diffusion of Zn^{2+} ions. These theoretical predictions were substantiated by experimental data acquired from hydrothermal synthesis, which indicated a marked increase in interlayer spacing. Significantly, the NVO-rGO composite exhibits remarkable cyclic durability, maintaining 95% of its initial specific capacity of 507 mAh g^{-1} after 600 cycles at a current density of 5 A g^{-1}. The electrochemical performance of NVO-rGO not only surpasses that of pristine NVO but also outperforms the majority of existing vanadium oxide cathode materials reported in the literature. This study underscores the effective integration of theoretical insights and experimental validation, contributing to the advancement of high-performance energy storage technologies.

Keywords: zinc-ion batteries; cathode materials; $NH_4V_4O_{10}$; reduced graphene oxide

1. Introduction

As global fossil fuel reserves continue to deplete, there is an urgent need to transition towards more sustainable energy infrastructures, emphasizing the harnessing of renewable energy sources such as wind and tidal energy [1,2]. A predominant challenge with these renewables is their inherent intermittency, which necessitates the development of efficient energy storage solutions—a critical topic in current scientific discourse. Over the past decade, lithium-ion batteries (LIBs) have become a central technology in this field, attracting significant interest due to their high energy density and commendable cycle life [3,4], thus establishing their dominance in the domain of electrochemical energy storage. However, concerns about the limited availability of lithium, rising costs, and potential safety risks associated with organic electrolytes have been highlighted [5,6]. As a result, there is an increasing focus among researchers on exploring alternative battery technologies that offer ecological sustainability, cost-effectiveness, and inherent safety.

In the evaluation of diverse battery technologies, aqueous zinc-ion batteries (AZIBs) have emerged as a notable contender. Their increasing prominence is attributed to several advantageous attributes: abundant global zinc reserves, the environmentally benign nature of its utilization, a commendable theoretical specific capacity of 820 mAh g^{-1}, and a favorable redox potential of −0.76 V versus the Standard Hydrogen Electrode (SHE) [7,8]. Despite these advantages, the technology faces significant challenges. A primary issue is the pronounced electrostatic interactions between Zn^{2+} ions and electrode materials [9]. These interactions create substantial potential energy barriers during the intercalation and de-intercalation of Zn^{2+} ions, leading to structural degradation in cathode materials through repeated charge-discharge cycles [10].

 doi:10.20944/preprints202405.0122.v2

The cathode plays a crucial role in determining the electrochemical performance of batteries, particularly in the case of aqueous zinc-ion batteries (AZIBs). Consequently, developing high-performance cathode materials that facilitate rapid Zn^{2+} migration and exhibit high capacity is essential for the practical implementation of AZIBs. A variety of cathode materials, including manganese (Mn)-based [11–13], vanadium (V)-based compounds [14,15], and Prussian blue analogs [16,17], have been extensively investigated. Among these, vanadium-based oxides are distinguished by their range of oxidation states from V^{2+} to V^{5+}. This variability in oxidation states provides greater structural and coordination flexibility, and the possibility for multi-electron transfer, which can lead to enhanced specific capacities [18]. However, the diversity of these oxidation states also presents challenges, including slow reaction kinetics and complex reaction mechanisms that can hinder performance.

Despite these challenges, AZIBs exhibit considerable potential and promise for future energy storage systems. Nonetheless, widespread practical application requires ongoing research to overcome the aforementioned obstacles. V_2O_5, a well-known layered vanadium-based cathode material, demonstrates excellent electrochemical performance. Its derivative, $NH_4V_4O_{10}$ (NVO), not only retains the benefits of V_2O_5 but also enhances the stability of the layered structure through the formation of N-H-O hydrogen bonds between the [VO_6] octahedra [19–23].

Despite these promising attributes, the cyclic and rate performances of NVO remain less than optimal. Density Functional Theory (DFT) calculations indicate that incorporating reduced graphene oxide (rGO) with NVO can enhance the interlayer spacing of the material. Additionally, rGO serves a protective role, reducing the charge transfer interactions between Zn^{2+} ions and the vanadium oxide matrix, thus facilitating improved Zn^{2+} diffusion. Following these theoretical predictions, NVO was composited with rGO using a hydrothermal synthesis method. The experimental results confirmed the theoretical predictions, showing an increase in interlayer spacing. At a current density of 0.2 A g^{-1}, the initial specific capacity was recorded at 507 mAh g^{-1}. Remarkably, after enduring 600 cycles at an elevated current density of 5 A g^{-1}, the composite material maintained 95% of its initial capacity.

2. Results and Discussion

2.1. DFT Calculations

In order to investigate the effects of rGO composite on the NVO system, we conducted a series of Density Functional Theory (DFT) calculations. We constructed models for Zn^{2+} embedded in pristine NVO (Zn-NVO) and Zn^{2+} embedded in an NVO system composited with rGO (Zn-NVO@rGO). Both systems were subjected to stringent structural optimizations, the outcomes of which are illustrated in Figure 1a and Figure 1c, respectively. These figures highlight the expansion in interlayer spacing subsequent to the incorporation of rGO, which facilitates the diffusion of Zn^{2+} ions.

To further examine the specifics of Zn charge transfer, we calculated the charge density difference, as depicted in Figure 1b and Figure 1d. In these visual representations, blue regions denote areas where charge density around Zn^{2+} has decreased, whereas yellow regions indicate an increase in charge density. It is important to note that in the pristine NVO system, there is a discernible charge transfer between Zn^{2+} and the oxygen atoms in the V-O bonds across two distinct layers. This transfer results in strong electrostatic interactions between Zn^{2+} and the host material, which hinders the diffusion of Zn^{2+} ions.

However, the introduction of rGO significantly alters this dynamic. rGO serves as a shielding layer, reducing the extent of charge transfer to only the oxygen in the V-O bonds of one layer of the NVO system. This reduction in charge transfer weakens the electrostatic interactions between Zn^{2+} and the vanadium oxide host, thereby promoting the diffusion of Zn^{2+} ions and enhancing the electrochemical performance of the Zn-NVO@rGO system. These DFT calculations are instrumental in providing a microscopic view of the electronic interactions and structural changes induced by the addition of rGO.

 doi:10.20944/preprints202405.0122.v2

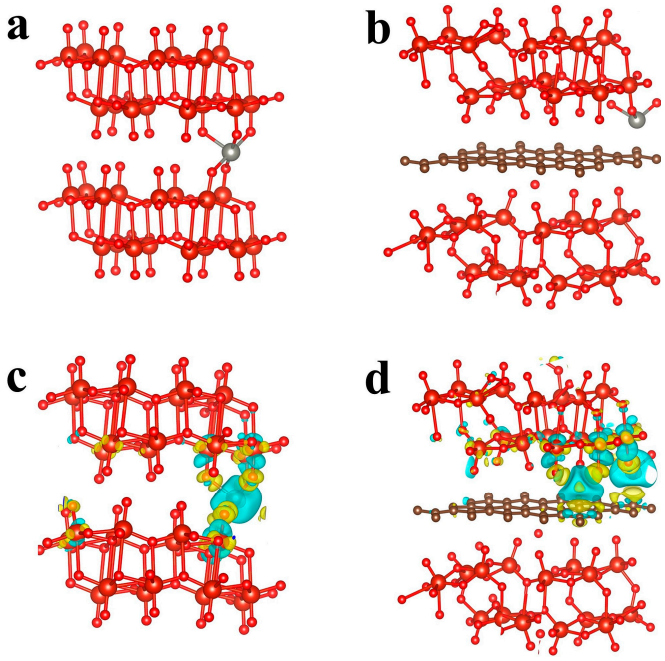

Figure 1. Optimized structure of (**a**) Zn-NVO and (**b**) Zn-NVO@rGO, charge density difference of (**c**) Zn-NVO and (**d**) Zn-NVO@rGO.

2.2. Morphological Characterization

To validate the outcomes of DFT calculations, we synthesized NVO and NVO@rGO composites via a single-step hydrothermal method. The structural compositions of these materials were analyzed using X-ray Powder Diffraction (XRD). As depicted in Figure 2a, the XRD patterns of NVO@rGO align well with the reference pattern of NH4V4O10 (JCPDS 31-0075), showcasing characteristic peaks at 7.44°, 25.06°, 30.32°, 45.84°, and 48.6° which correspond to the standard peaks of NVO. The XRD analysis confirmed that the synthesized NVO closely matched the $NH_4V_4O_{10}$ standard as well.

Notably, the (001) plane peak of NVO@rGO demonstrated a shift towards lower angles, transitioning from 9.6 Å to 11.87 Å, suggesting an increase in the interlayer spacing. This observation aligns with our DFT predictions and indicates enhanced intercalation capabilities, potentially facilitating improved ion diffusion pathways, crucial for the electrochemical performance of the composite material. However, primarily based on the observed increase in interplanar spacing from DFT predictions and XRD analysis, it is insufficient to conclusively demonstrate graphene's integration into the NVO crystal structure. Other intercalated species such as water or ammonium ions might also contribute to the altered interplanar spacing. Consequently, we propose that the formation of a composite structure is a more plausible scenario for the observed phenomena.

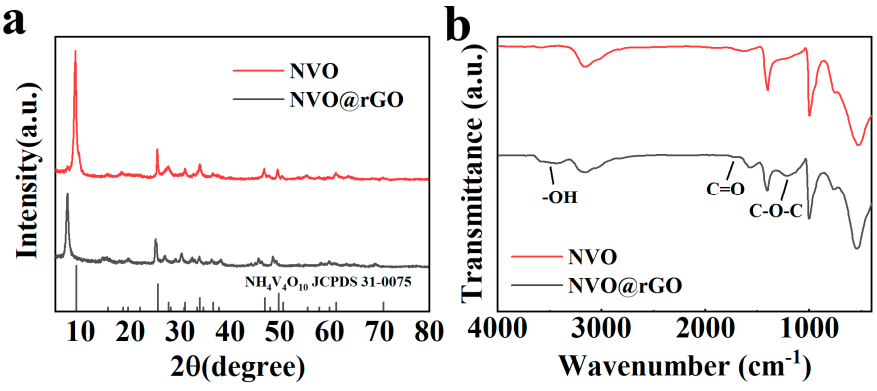

Figure 2. (**a**) XRD patterns and (**b**) FTIR spectrum of NVO, NVO@rGO.

 doi:10.20944/preprints202405.0122.v2

In addition to X-ray diffraction, Fourier Transform Infrared Spectroscopy (FTIR) was employed to further investigate the structural composition of NVO and NVO@rGO. As depicted in Figure 2b, both materials exhibited similar FTIR spectra, indicating a preservation of the base structural features upon rGO integration. However, the spectrum for NVO@rGO displayed several additional, albeit weaker, absorption peaks that are characteristic of rGO functional groups. Specifically, the absorption peak at 3436 cm^{-1} is attributed to the stretching vibrations of –OH groups, indicative of residual hydroxyl functionalities or absorbed water molecules. The peak at 1728 cm^{-1} corresponds to the C=O stretching vibrations, typically found in carboxylic acid groups or ketones, while the peak at 1222 cm^{-1} represents the C–O–C vibrations, which are commonly associated with ethers or esters. The relative weakness of these oxygen-containing functional group peaks suggests incomplete reduction of the graphene oxide to rGO.

Furthermore, Raman spectroscopic analysis was conducted on the NVO@rGO composite, with the results depicted in Figure 3. The Raman spectrum exhibited two distinct peaks at 1347 cm^{-1} and 1594 cm^{-1}, corresponding to the in-plane vibrations of sp^2 hybridized carbon atoms (D band) and the stretching vibrations of sp^2 hybridized carbon atoms in conjunction with π electrons (G band), respectively. These spectral features indicate the incorporation of rGO within the composite.

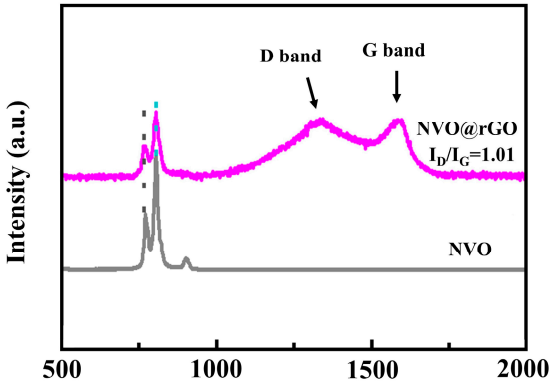

Figure 3. Raman patterns of NVO and NVO@rGO.

The intensity ratio of the D band to the G band (I_D/I_G), a metric of defect density and graphitization level, was calculated to be 1.01 for the NVO@rGO composite. This I_D/I_G ratio indicates a well-balanced graphitization with a moderate level of defects, which supports the favorable electrochemical properties observed in this study.

Scanning Electron Microscopy (SEM) was utilized to investigate the microstructural morphology and elemental composition of the synthesized NVO@rGO composite. Images presented in Figure 4a and Figure 4b reveal that NVO@rGO consists of uniform ultrathin nanosheets. The ultrathin structure is advantageous for enhancing the surface area available for electrochemical reactions and facilitates rapid ion transport.

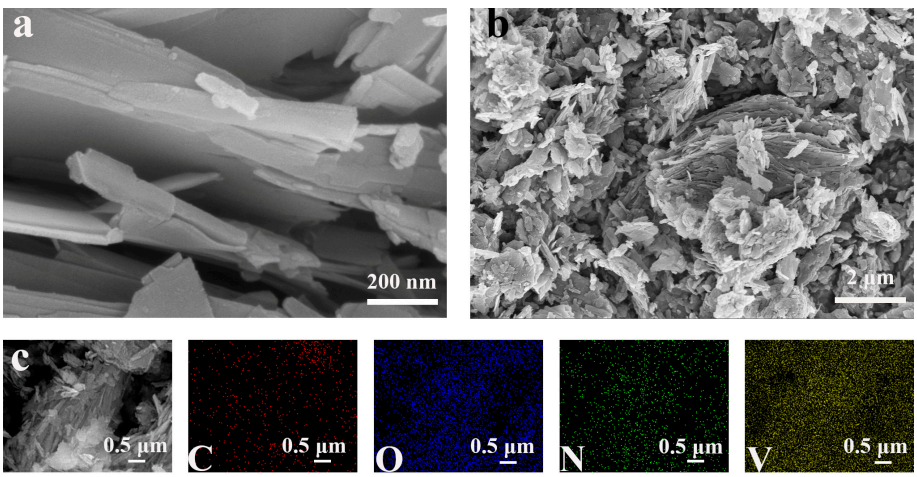

 doi:10.20944/preprints202405.0122.v2

Figure 4. (**a**–**b**) SEM patterns of NVO@rGO; (**c**) EDS mapping of NVO@rGO.

Further analysis using SEM Energy-Dispersive X-ray Spectroscopy (EDS) mapping (shown in Figure 4c) confirmed the homogeneous distribution of carbon (C), oxygen (O), nitrogen (N), and vanadium (V) elements within the composite. The presence of these elements in a uniformly distributed manner indicates effective incorporation of rGO into the NVO matrix. This homogeneous distribution is crucial for ensuring consistent electrochemical behavior across the material, which is essential for the stability and reliability of battery performance.

To gain further insight into the microstructural details of NVO@rGO, Transmission Electron Microscopy (TEM) was employed. The TEM images, as shown in Figures 5a and 4b, distinctly reveal the nanosheet morphology of the composite. These images also clearly demonstrate the uniform coating of rGO on the NVO cathode material. The high-resolution TEM (HRTEM) images, displayed in Figure 5c, distinctly show the lattice fringes of NVO@rGO, with a lattice spacing of 0.198 nm that corresponds to the (–205) plane of NVO. This precise observation of lattice fringes underscores the crystalline nature of the NVO within the composite and supports the structural integrity of the material even after the incorporation of rGO.

Furthermore, the Selected Area Electron Diffraction (SAED) patterns, presented in Figure 5d, exhibit a ring-like diffraction pattern typical of polycrystalline materials. This pattern clearly resolves the diffraction rings corresponding to the (400), (001), and (110) planes of NVO, indicating that the crystalline phases of NVO are well-preserved within the composite. The presence of these distinct diffraction rings also helps confirm the phase purity and crystalline quality of the material, which are essential for predictable and stable electrochemical performance.

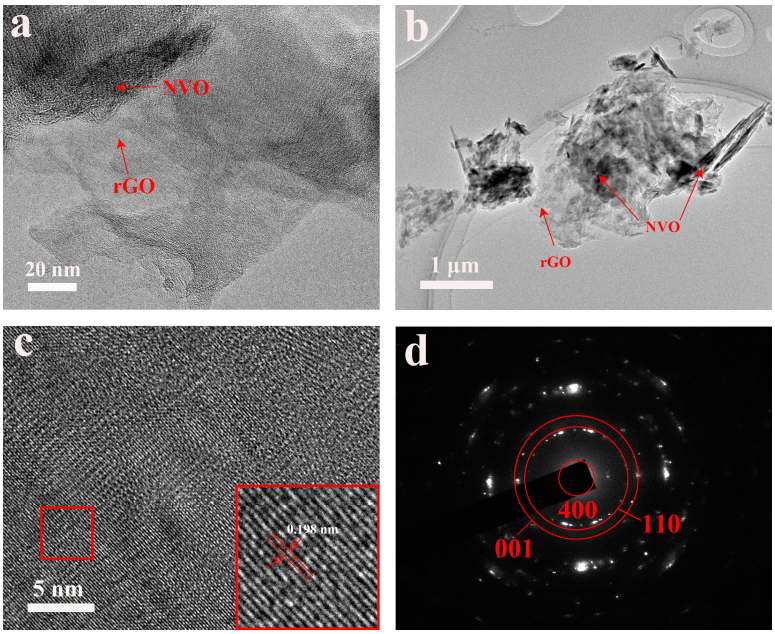

Figure 5. (**a**–**b**) TEM images, (**c**) lattice fringes and (**d**) SAED patterns of NVO@rGO.

2.3. Electrochemical Properties Characterization

To evaluate the electrochemical behavior of NVO@rGO in reaction processes, the material was assembled into a coin cell for electrochemical performance testing. Cyclic voltammetry (CV) scans were initially performed at a scan rate of 0.1 mV s^{-1} (illustrated in Figure 6a), where a good overlap is observed in the CV curves from the second to the fourth cycle, indicating a good cyclic stability. The presence of multiple oxidation and reduction peaks within these curves confirmed that the electrochemical reactions of NVO@rGO are complex and involve multiple steps. Specifically, the oxidation and reduction peaks at 1.5 V and 1.3 V respectively, are associated with the intercalation and deintercalation of NH_4^+ ions [24–26], highlighting the active role of ammonium in the electrochemical process.

 doi:10.20944/preprints202405.0122.v2

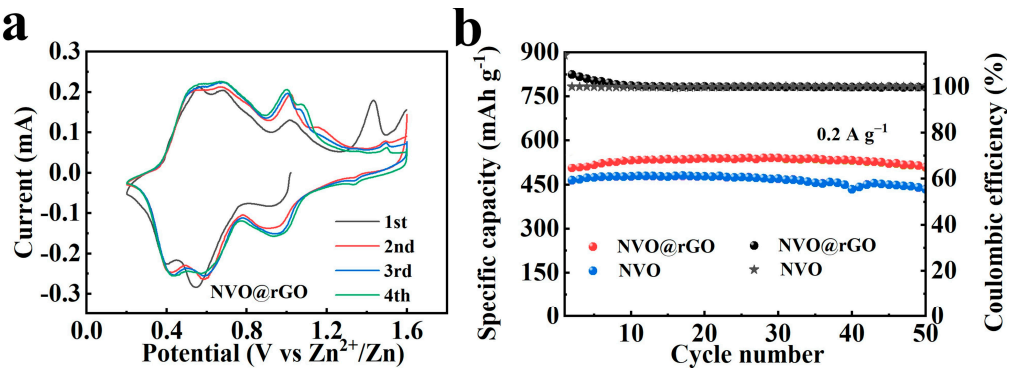

Figure 6. (**a**) CV curves of NVO@rGO; (**b**) Cycling performance plots of NVO and NVO@rGO at a current density of 0.2 A g^{-1}.

Subsequently, the cycling performance of both NVO and NVO@rGO was tested at a current density of 0.2 A g^{-1} (shown in Figure 6b). The initial specific capacity of NVO was recorded at 464 mAh g^{-1}, with a capacity retention of 94% after 50 cycles. In comparison, NVO@rGO exhibited a higher initial capacity of 507 mAh g^{-1} and an exceptional capacity retention of 100% after the same number of cycles. This improvement in both initial capacity and retention for NVO@rGO compared to pristine NVO is a testament to the beneficial effects of rGO integration, which enhances the structural stability and electrochemical reactivity of the material. These results are in line with the predictions from DFT calculations, which suggested that the addition of rGO would facilitate better ion diffusion and charge transfer.

Moreover, the performance of NVO@rGO not only surpasses that of pristine NVO but also exceeds most of the vanadium oxide cathode materials reported in current literature (as shown in Table 1). This superior performance can be attributed to the structural and electronic enhancements brought about by the incorporation of rGO into the NVO matrix, which optimize the material's electrochemical properties.

Table 1. Comparison with reported electrochemical properties of vanadium oxidation chemicals.

Cathode materials	Electrochemical performance (Capacity retention, cycle numbers)	Reference
NVO@rGO	507 mAh g^{-1} at 0.2 A g^{-1} (100%, 50 cycles)	This work
$(NH_4)_{0.37}V_2O_5{\cdot}0.15H_2O$	398 mAh g^{-1} at 0.5 A g^{-1} (90%, 50 cycles)	[26]
$KNH_4V_4O_{10}$	405 mAh g^{-1} at 0.4 A g^{-1} (92.1%, 100 cycles)	[27]
Cs-V_2O_5	369 mAh g^{-1} at 0.1 A g^{-1} (90%, 200 cycles)	[28]
$(NH_4)_xV_2O_5{\cdot}nH_2O$	372 mAh g^{-1} at 0.1 A g^{-1} (63%, 50 cycles)	[29]
$Zn_3V_2MoO_8$	337 mAh g^{-1} at 0.2 A g^{-1} (90%, 70 cycles)	[30]
$NaCaV_2O_5$	310 mAh g^{-1} at 0.5A g^{-1} (100%, 200 cycles)	[31]
$(NH_4)_2V_4O_9$	493 mAh g^{-1} at 0.2 A g^{-1} (83.2%, 100 cycles)	[32]
V_3O_7/V_6O_{13}	415 mAh g^{-1} at 0.1 A g^{-1} (73%, 100 cycles)	[33]
$Na_2V_6O_{16}{\cdot}3H_2O$	401 mAh g^{-1} at 0.3 A g^{-1} (91.8%, 300 cycles)	[34]
O_d-HNaVO@rGO	380 mAh g^{-1} at 0.5 A g^{-1} (97.4%, 200 cycles)	[35]

Figure 7 presents the galvanostatic charge-discharge (GCD) curves for NVO@rGO and NVO at a current density of 0.2 A g^{-1}. The curves exhibit similar shapes, indicating analogous electrochemical processes are underway in both samples. The high degree of overlap in the GCD curves suggests that both materials, NVO@rGO and NVO, exhibit excellent cyclic stability. This similarity in electrochemical behavior can be attributed primarily to the inherent properties of NVO in both cases.

Furthermore, Figure 7a distinctly illustrates the charge and discharge capacities of the NVO@rGO composite, noting a significant observation in the initial cycle where the charge capacity exceeds the discharge capacity. This phenomenon substantiates the premise that the Coulombic

 doi:10.20944/preprints202405.0122.v2

efficiency in the first cycle is inherently less than 100%, a conclusion that appears to contradict the cycling performance data presented in Figure 6b. The discrepancy can be attributed to a misinterpretation of the transient phase behavior depicted in Figure 6b as reflective of a stable Coulombic efficiency. In contrast, Figure 7a provides the raw capacity data, emphasizing that the excess in charge capacity over discharge capacity is due to initial material activation and ion trapping processes. These findings underscore the necessity of considering the dynamic changes in material behavior during initial cycles to accurately assess the electrochemical performance of the NVO@rGO composite.

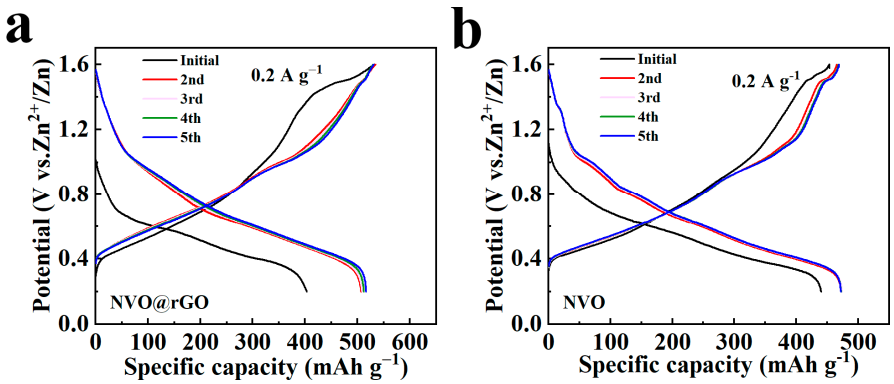

Figure 7. GCD curves of (**a**) NVO@rGO and (**b**) NVO at a current density of 0.2 A g^{-1}.

Figure 8 showcases the rate performance of NVO@rGO compared to NVO, as the current density was increased stepwise from 0.2 A g^{-1} to 5 A g^{-1}. The specific capacities for NVO@rGO at these current densities were recorded at 495, 494, 491, 470, and 401 mAh g^{-1} respectively. Notably, when the current density was reverted back to 0.2 A g^{-1}, the specific capacity of NVO@rGO impressively recovered to 518 mAh g^{-1}. This recovery and the overall higher capacities at each rate compared to NVO underscore the superior rate capability and resilience of the composite material.

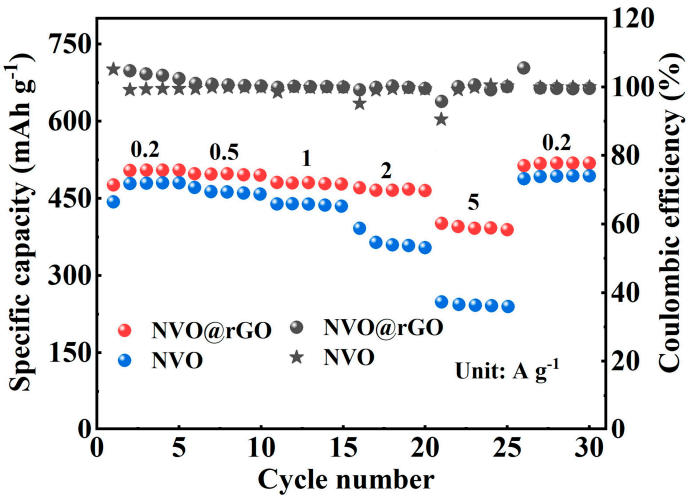

Figure 8. Rate performance graph of NVO@rGO and NVO.

The enhanced performance of NVO@rGO can be attributed to the incorporation of rGO, which not only improves the electrical conductivity of NVO but also serves as a structural scaffold. This scaffold helps in stabilizing the crystal structure of NVO during electrochemical cycling, mitigating volume expansion that often leads to rapid capacity fade in such materials. Additionally, the presence of rGO likely facilitates better electron and ion transport within the electrode, enhancing both the rate capability and cycling stability.

Long-term cycling performance, illustrated in Figure 9, further highlights the durability of NVO@rGO. Tested at a high current density of 5 A g^{-1}, NVO@rGO demonstrated an initial specific

 doi:10.20944/preprints202405.0122.v2

capacity of 388 mAh g^{-1} and maintained a retention rate of 95% after 600 cycles. In contrast, NVO showed a significantly lower capacity retention under the same conditions. This superior performance of NVO@rGO is indicative of its potential in applications requiring high power outputs and long-term reliability.

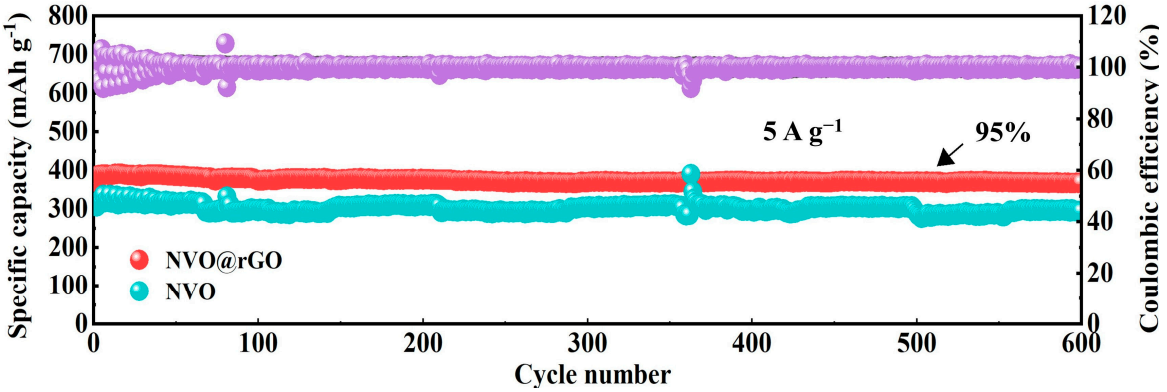

Figure 9. Cycling performance of NVO@rGO, NVO at current density of 5 A g^{-1}.

To further elucidate the underlying electrochemical reaction mechanisms, CV curves were examined at various scan rates across a potential window of 0.2 to 1.6 V. Figure 10 illustrates the CV profiles for NVO@rGO and NVO, which exhibit similar morphologies, suggesting that analogous electrochemical processes occur within both materials. Notably, as the scan rate increases, both the oxidation and reduction peaks demonstrate shifts of varying magnitudes, a behavior indicative of electrochemical polarization.

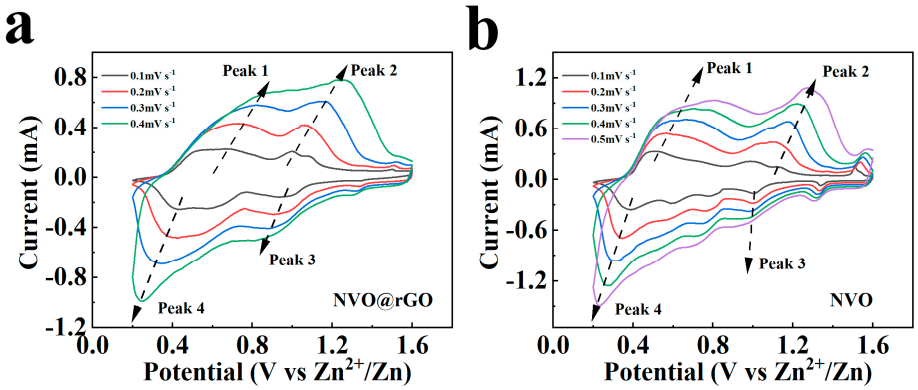

Figure 10. CV curves of (**a**) NVO@rGO and (**b**) NVO at various scan rates.

In these CV analyses, the relationship between the peak current (i) and the scan rate (v) is described by the following equations:

$$i = av^b \quad (1)$$

$$\log(i) = \log(a) + b\log(v) \quad (2)$$

where a and b are constants determined empirically. The coefficient b is particularly informative, indicating the degree to which the electrochemical reactions are governed by diffusion or capacitive processes. Generally, b values that are close to 0.5 suggest a reaction mechanism dominated by diffusion, whereas values approaching 1 imply predominant capacitive control.

The calculated b values, as presented in Figures 11a and 11b, for the four distinct peaks of NVO@rGO are 0.81, 0.97, 0.84, and 0.96, and for NVO are 0.73, 1, 0.86, and 0.78, respectively. These values, all within the range of 0.5 to 1, confirm that ion transport within these materials is influenced by both diffusion and surface capacitive effects. However, the prevalence of values nearing 1

 doi:10.20944/preprints202405.0122.v2

highlights that capacitive contributions play a significant role in defining their overall capacitance behavior.

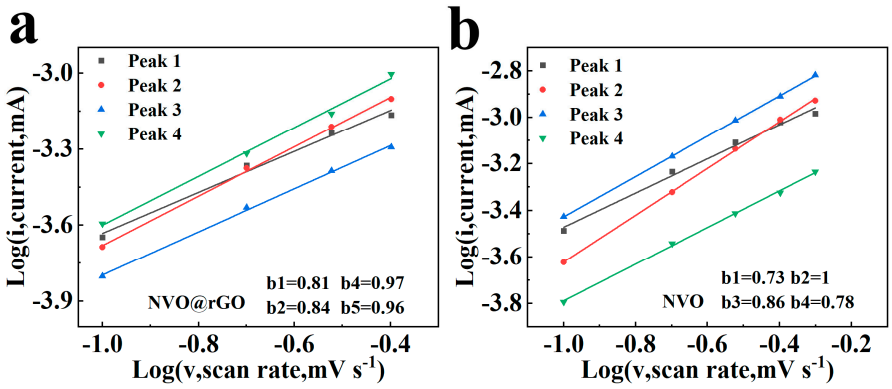

Figure 11. *b*-value curves of (**a**) NVO@rGO and (**b**) NVO.

Electron Paramagnetic Resonance (EPR) testing, depicted in Figure 12a, has provided critical insights into the presence of oxygen vacancies within the NVO@rGO composite. These vacancies play a multifaceted role in enhancing the electrochemical properties of zinc-ion batteries [36,37]. Oxygen vacancies are known to amplify the number of available active sites on the electrode material, which are pivotal for Zn^{2+} adsorption and storage. This augmentation is crucial as it directly contributes to reducing the ion adsorption barriers, thereby facilitating smoother Zn^{2+} diffusion across the electrode material.

The strategic increase in active sites due to oxygen vacancies accelerates electron transfer kinetics, which is instrumental in improving the overall electrochemical performance and structural stability of the battery. This dynamic is essential for maintaining the integrity of the electrode material through numerous charging and discharging cycles, as it mitigates the typical degradation associated with repeated electrochemical cycling.

Furthermore, oxygen vacancies contribute to structural modifications within the material matrix. They facilitate the creation of new pathways for ion insertion, which are not typically available in defect-free materials. These new pathways significantly improve the reaction reactivity, enhancing the battery capacity substantially. Such structural enhancements also induce a crucial transition in the material from semiconductive to conductive behavior, which in turn markedly enhances the charge transfer efficiency across the electrode. This transition is fundamental for high-performance battery applications, as it ensures a more efficient and rapid charge-discharge cycle.

Most notably, the expanded availability of active sites, which are beneficial for anchoring Zn^{2+} ions, leads to an increase in the electrochemically active surface area. This increase is directly linked to enhanced pseudocapacitance, thereby raising the battery's overall capacity. The correlation between increased active surface area and battery capacity underscores the importance of oxygen vacancies in developing advanced battery materials that offer higher energy densities and longer life cycles.

 doi:10.20944/preprints202405.0122.v2

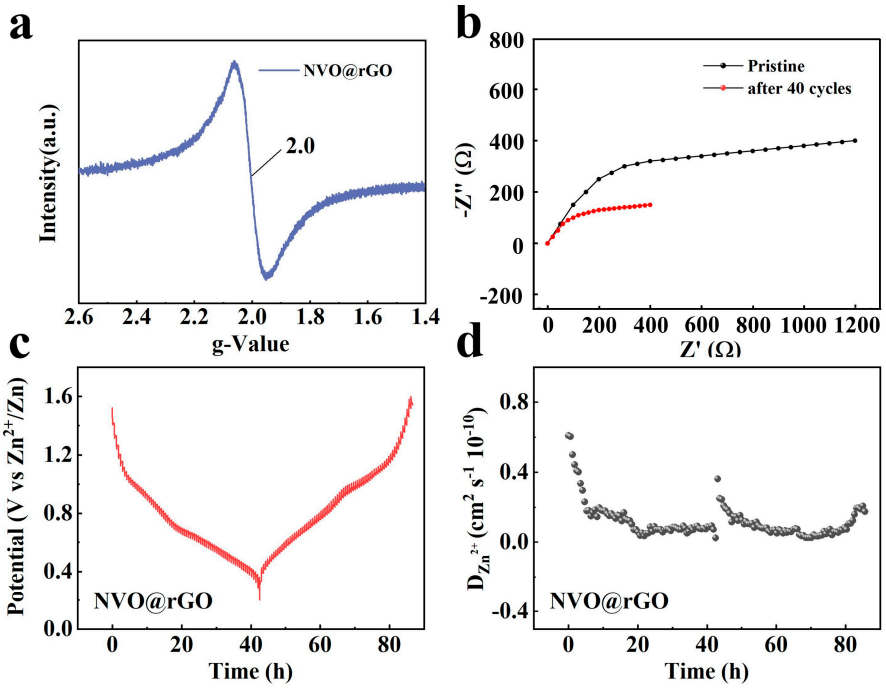

Figure 12. (**a**) EPR profiles, (**b**) EIS profiles and (**c**–**d**) GITT profiles of NVO@rGO.

Further investigation into the electrochemical properties of the NVO@rGO composite was undertaken via Electrochemical Impedance Spectroscopy (EIS). EIS measurements were conducted over a frequency range from 0.01 Hz to 100 kHz, across various cycling intervals, as depicted in Figure 12b. The Nyquist plots obtained illustrate significant alterations in impedance characteristics both pre- and post-cycling, providing insights into the mechanisms influencing performance. Initially, the EIS spectra displayed a pronounced semicircular region at high frequencies, indicative of the charge transfer resistance at the electrode-electrolyte interface. A notable diminishment in the semicircle's presence was observed post-cycling, suggesting a decrease in charge transfer resistance. This observed decrease is generally associated with the formation of more efficient electron conduction pathways, potentially due to the restructuring of the electrode material during cycling. Such improvements in charge transfer efficiency indicate that the NVO@rGO composite may undergo electrochemical activation, thereby enhancing its electrical conductivity and overall electrochemical reactivity.

Furthermore, the linear region observed at low frequencies, corresponding to the Warburg impedance, is indicative of ionic diffusion resistance within the electrode. The slope of this region changes after cycling, pointing to alterations in the ionic transport dynamics. This change is likely due to modifications in the microstructure of the electrode material, which enhance ion transport pathways, thereby reducing diffusion resistance.

In addition, the electrochemical performance of zinc-ion batteries is significantly influenced by the properties of zinc anodes, particularly through their interactions with cathode materials. Throughout the cycling process, zinc anodes are pivotal in maintaining a dynamic equilibrium at the interfacial layer, as the processes of zinc dissolution and deposition critically govern the overall interfacial resistance. Notably, the incorporation of rGO within the NVO@rGO cathode architecture plays a vital role in stabilizing zinc deposition. This stabilization is achieved by promoting a more uniform distribution of the electric field across the interface, thereby reducing localized current densities and minimizing dendritic growth. Such enhancements in interfacial stability lead to a decrease in interfacial resistance throughout the battery's cycling. Consequently, this contributes to improved battery efficiency and extended cycle life.

The Galvanostatic Intermittent Titration Technique (GITT) was utilized to quantify the diffusion coefficient of Zn^{2+} ions in the NVO@rGO composite, providing a quantitative measure of ion mobility critical for electrochemical applications. The GITT experiments were methodically carried out

 doi:10.20944/preprints202405.0122.v2

through a series of pulses followed by a constant current operation and a subsequent relaxation period. Specifically, a current density of 0.1 A g^{-1} was applied, with a relaxation time set at 30 minutes, and measurements were taken at 10-second intervals. The calculation is based on the following equation:

$$D^{GITT} = \frac{4}{\pi\tau}\left(\frac{m_B V_M}{M_B S}\right)^2 \left(\frac{\Delta E_S}{\Delta E_t}\right)^2 \quad (4)$$

where τ represents the relaxation time, m_B is the mass of active material, V_M denotes the molar volume, M_B is the molar mass, S is the surface area of the electrode, ΔE_S and ΔE_t are the steady-state and transient potential changes, respectively. Using this model, we calculated the diffusion coefficient of Zn^{2+} ions to be 10^{-11} cm^2 s^{-1}. This value indicates the mobility of Zn^{2+} ions within the NVO@rGO matrix, which is crucial for assessing the efficiency of ion transport.

2.4. Storage Mechanism of Zn^{2+}

To further investigate the zinc storage mechanism within the NVO@rGO system during electrochemical reactions, analyses were carried out using ex situ XRD and ex situ X-ray photoelectron spectroscopy (XPS). A button cell employing 3 M $Zn(CF_3SO_3)_2$ as the electrolyte was assembled and subjected to ten cycles of charging and discharging. Subsequently, the electrode was extracted, washed with distilled water, and dried prior to XRD examination. The results, presented in Figure 13, show characteristic peaks at 7.44°, 25.06°, 30.32°, 45.84°, and 48.6°. These peaks correspond to the standard diffraction angles for $NH_4V_4O_{10}$, aligning with the (001), (110), (–311), (–205), and (020) crystallographic planes, respectively. The persistence of these peaks throughout the cycling process suggests that the incorporation of reduced graphene oxide (rGO) does not modify the fundamental reaction dynamics within the battery. Notably, the emergence and dissolution of new phases were observed across the entire charging and discharging cycles, indicating dynamic changes in the electrode structure.

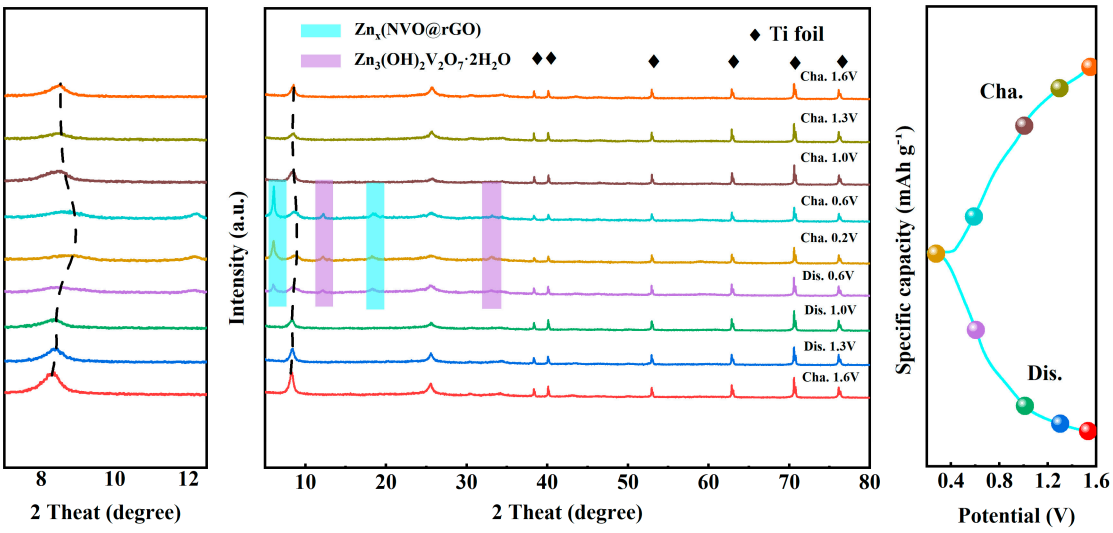

Figure 13. Ex-situ XRD patterns of NVO@rGO at different charge states during the 10th cycle.

In Figure 13, the left portion presents an enlarged view of the (001) crystallographic plane of NVO@rGO. Notably, the peak corresponding to the (001) plane shifts toward higher diffraction angles as the electrode transitions from a charged state at 1.6 V to a discharged state at 0.2 V. This shift indicates a reduction in interlayer spacing, which is attributed to the electrostatic interactions between Zn^{2+} ions and the bilayer structure. When the electrode is returned to the fully charged state at 1.6 V, the peak relocates to its original position, affirming the structural integrity of the NVO@rGO electrode. This resilience is ascribed to the mechanical support and enhanced electrical conductivity provided by graphene within the composite.

Additionally, the XRD data reveal the appearance and subsequent disappearance of two distinct sets of diffraction peaks during the discharge to 0.6 V and recharge to the same voltage. The first set

 doi:10.20944/preprints202405.0122.v2

of peaks, located at 5.98° and 18.32°, is associated with the intercalation and deintercalation of Zn^{2+} ions within the NVO@rGO electrode matrix. These peaks disappear as the Zn^{2+} ions are extracted at 0.6 V. A second set of peaks, observed at 12.08° and 33.2°, corresponds to the formation of a new phase, $Zn_3(OH)_2V_2O_7{\cdot}2H_2O$. This phase is a recognized intermediate in the electrochemical processes of vanadium-based AZIBs [38,39], underscoring the dynamic nature of the phase transformations occurring within these cells.

To confirm the presence of the specified compound, SEM analyses were performed on electrodes in their initial state, after discharge to 0.2 V, and following recharge to 1.6 V (Figures 14a–c). The SEM images of the electrode in its initial state showed no extraneous materials. However, upon discharge to 0.2 V, micrometer-scale flake-like structures emerged on the surface of the active material. These structures are consistent with the morphology of $Zn_3(OH)_2V_2O_7{\cdot}2H_2O$, as described in existing literature [40]. These structures dissipated upon recharging to 1.6 V, aligning with changes observed in ex-situ XRD analyses and demonstrating the reversible intercalation and deintercalation of Zn^{2+} ions throughout the cycling process. To further verify the identity of the intermediate phase, the battery was discharged to 0.2 V, and EDS mapping of the micrometer-scale flakes on the electrode was conducted (Figure 14d). The EDS analysis indicated a uniform distribution of Zn, V, and O elements within these structures, confirming their composition as $Zn_3(OH)_2V_2O_7{\cdot}2H_2O$. Additionally, the presence of these by-products led to the formation of uniform holes on the surface of the cathode plate, a morphological alteration that likely increases the contact area available for electrochemical reactions and potentially enhances the system's electrochemical performance.

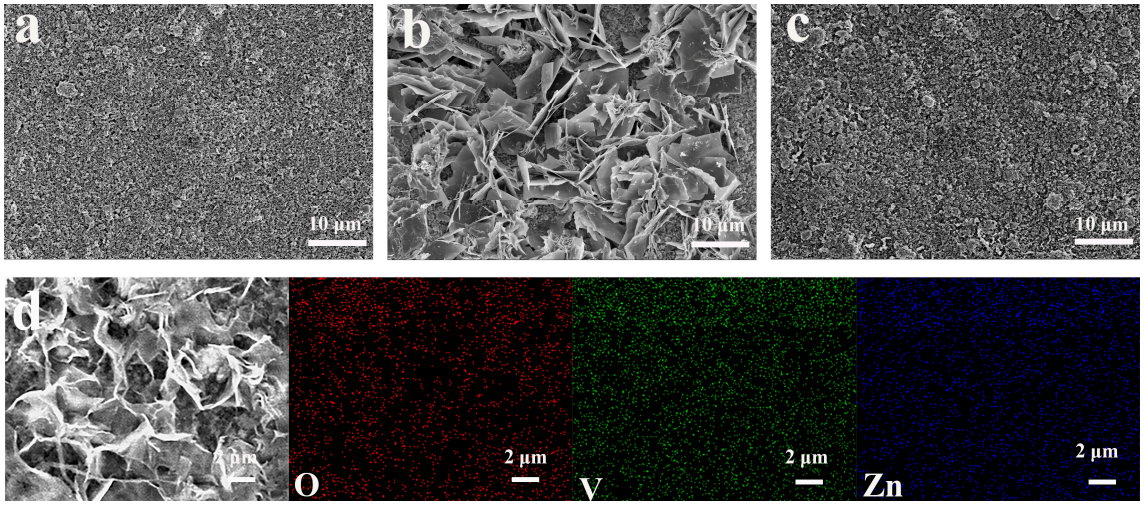

Figure 14. (**a–c**) SEM patterns of NVO@rGO under different discharge states; (**d**) Elemental mapping patterns of NVO@rGO under discharge to 0.2 V.

Concurrently, XPS analyses were performed on electrodes in various states: pristine, after discharging to 0.2 V, and after recharging to 1.6 V (Figure 15), to elucidate the chemical state transformations of the cathode material during the electrochemical process. Initially, four prominent peaks were detected: V $2p_{1/2}$ and V $2p_{3/2}$ at 516.39 eV and 523.90 eV respectively, characteristic of V^{4+}, and V $2p_{1/2}$ and V $2p_{3/2}$ at 517.72 eV and 525.26 eV respectively, indicative of V^{5+}. Upon discharging to 0.2 V, an increase in the intensity of V^{4+} peaks was observed, signaling a reduction state favorability. Further, during the discharge to 0.2 V, the vanadium-based cathode material underwent dissolution in the aqueous solution, resulting in the formation of the byproduct $Zn_3(OH)_2V_2O_7{\cdot}2H_2O$ [41]. Subsequent recharging to 1.6 V led to the predominance of V^{5+} over V^{4+}, reverting to the initial electrochemical state and demonstrating the structural reversibility of the cathode material.

In addition, the zinc states were monitored across different levels of discharge. Initially, no peaks corresponding to Zn^{2+} were discernible. Nevertheless, upon discharging to 0.2 V, peaks at 1022.7 eV and 1045.56 eV corresponding to Zn $2p_{1/2}$ and Zn $2p_{3/2}$ manifested, suggestive of Zn^{2+} intercalation. Notably, a residual absorption peak for zinc persisted upon recharging to 1.6 V. This occurrence is a

 doi:10.20944/preprints202405.0122.v2

typical reaction artifact, arising from incomplete extraction of Zn^{2+}, thereby resulting in the formation of residual, or "dead" zinc.

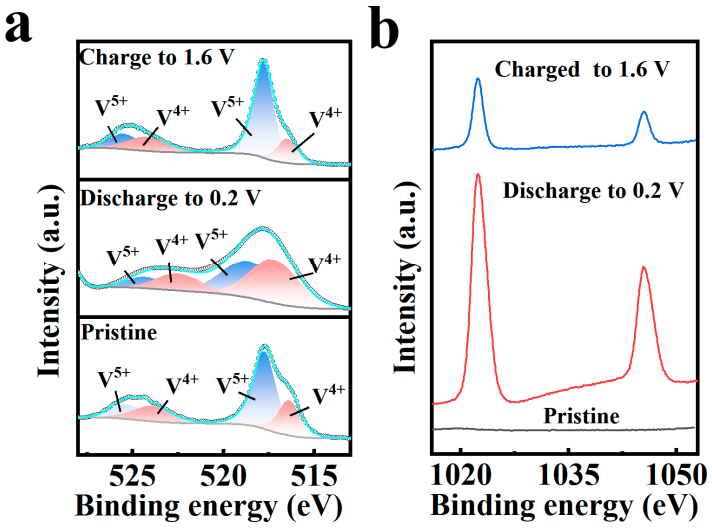

Figure 15. XPS patterns of (**a**) V 2p and (**b**) Zn 2p in the initial state, charging at 1.6 V and discharging at 0.2 V.

3. Materials and Methods

3.1. Calculation Method

The DFT calculations were performed using the Vienna Ab Initio Simulation Package (VASP) [42]. The exchange-correlation interactions were described by the Perdew–Burke–Ernzerhof (PBE) functional [43]. Our computational strategy incorporated a plane-wave basis set, with a chosen energy cutoff of 400 eV, in conjunction with the Projector Augmented Wave (PAW) method [44,45]. We set the convergence thresholds for the self-consistent field iterations at 1×10^{-5} eV, and for the force convergence at 0.01 eV $Å^{-1}$. The Brillouin zone was sampled using a Γ-centered k-point mesh of $2 \times 4 \times 1$ for both the relaxation of the geometric structures and the total energy calculations.

3.2. Preparation of Material

The synthesis of NVO and NVO@rGO was accomplished through a one-step hydrothermal method. Initially, NVO was synthesized by dissolving 8 mmol of ammonium metavanadate in 60 mL of deionized water, which was heated to 60°C until complete dissolution occurred. The solution was then allowed to cool to room temperature. In parallel, 8 mmol of oxalic acid was dissolved in 10 mL of deionized water and was slowly added to the ammonium metavanadate solution with continuous stirring. After vigorous stirring at room temperature for 0.5 hours, the combined solution was transferred to a 100 mL Teflon-lined autoclave and subjected to hydrothermal treatment at 180°C for 24 hours. Upon natural cooling to room temperature, the resultant dark green product was isolated in a centrifuge tube and washed multiple times with alternating cycles of deionized water and anhydrous ethanol, followed by centrifugation. The final product was then freeze-dried for 12 hours to yield NVO.

Subsequently, the NVO@rGO composite was synthesized by initially weighing 50 mg of graphene oxide (GO), which was then dispersed in 50 mL of distilled water. This mixture underwent sonication at a frequency of 45 kHz for 30 minutes to achieve a uniform dispersion of the GO. The GO utilized was sourced from Nanjing XFNANO Materials Tech Co., Ltd., located in Nanjing, China. The sonication process was meticulously monitored to ensure consistent dispersion throughout the solution. Then, 0.9359 g of NH_4VO_3 was added to this dispersion and dissolved at 60°C, after which the solution was allowed to cool to room temperature. Separately, 1.386 g of $H_2C_2O_4 \cdot 2H_2O$ was dissolved in 10 mL of distilled water. Once dissolved, it was slowly added to the graphene oxide solution containing NH_4VO_3 under vigorous stirring for 0.5 hours. This mixture was then transferred

 doi:10.20944/preprints202405.0122.v2

to a 100 mL Teflon-lined autoclave and subjected to a hydrothermal reaction at 180°C for 24 hours. After cooling to room temperature, the resultant black product was processed in the same manner as NVO, involving multiple washes, centrifugation, and freeze-drying, to yield the final product, designated as NVO@rGO.

3.3. Electrode Fabrication

The electrode composition comprising the active material, polyvinylidene fluoride (PVDF) as a binder, and acetylene black as a conductive agent, was added in a 6:3:1 ratio into a mortar. The mixture was ground extensively to ensure uniform blending and achieve a fine, smooth powder. Subsequently, N-methyl-2-pyrrolidone (NMP) was added dropwise, and the mixture was further milled until the resulting paste displayed a shiny surface. Titanium foil was employed as the current collector, onto which the paste was evenly spread. The coated foils were then dried in a vacuum oven at 110 °C for 12 hours. After cooling to room temperature, the electrodes were punched into circular disks of 1 cm diameter, with an active material load of approximately 1.3 mg cm^{-2}.

3.4. Structure and Morphology Characterization

The structural properties of all materials synthesized during the electrochemical process were characterized using XRD with Cu Kα radiation (Smart Lab SE, Tokyo, Japan). Morphological and crystalline features of these materials were systematically investigated using SEM (Hitachi SU8010, Tokyo, Japan) and TEM (FEI Talos F200X, Waltham, MA, USA). The elemental distribution within the samples was analyzed using SEM equipped with EDS. Additionally, XPS (Thermo ESCALAB 250Xi, Waltham, MA, USA) using an Al Kα anode was employed to determine the elemental composition and to monitor changes in the valence states in both powder samples and electrode slices.

Furthermore, FTIR, using a VERTEX 70 spectrometer (Saarbrücken, Germany), and employing the attenuated total reflectance (ATR) method, was utilized to elucidate the functional groups present within the materials. This approach facilitated comprehensive comparative analyses. Additionally, the presence of O_d in the materials was confirmed through EPR spectroscopy. These measurements were conducted using an EMX nano spectrometer, specifically designed for the detection of unpaired electrons.

3.5. Electrochemical Measurements

The electrochemical properties of the synthesized materials were extensively assessed through the assembly and evaluation of CR2032-type button cells, designated as the prototype cells for this study. During the assembly phase, zinc foil was employed as the anode, whereas titanium foil served as the current collector. A glass fiber material was utilized as the separator. The chosen electrolyte was a 3 M solution of zinc trifluoromethanesulfonate ($Zn(CF_3SO_3)_2$). The entire assembly process was conducted under standard atmospheric conditions and concluded with the cells being hermetically sealed using a specialized sealing apparatus.

CV and EIS measurements were performed using a CHI 760E electrochemical workstation. For the CV measurements, a voltage range of 0.2 to 1.6 V was applied at scan rates from 0.1 to 0.5 mV s^{-1}. EIS measurements were conducted across a frequency range of 0.01 Hz to 100 kHz in a potentiostatic mode with an amplitude of 10 mV. Further evaluations, including assessments of specific capacity, GCD curves, and GITT, were conducted using the Battery Test System CT2001A, produced by Wuhan LAND Electric Co., within the same voltage range of 0.2 to 1.6 V. For the GITT measurements, a constant current mode was employed, featuring a pulse duration of 10 minutes followed by a relaxation period of 1 hour.

4. Conclusions

This study presents a significant advancement in the development of AZIBs through the integration of a novel cathode material, NVO, with rGO. The introduction of rGO to the NVO structure, as hypothesized and supported by DFT calculations, effectively increases the interlayer

 doi:10.20944/preprints202405.0122.v2

spacing and reduces charge transfer interactions. This modification facilitates a more efficient diffusion of Zn^{2+} ions, addressing a crucial challenge in the performance of vanadium-based cathode materials. Experimental results from hydrothermal synthesis have validated our theoretical predictions, demonstrating a substantial increase in interlayer spacing. The electrochemical tests further highlight the remarkable durability of the NVO-rGO composite, which retains 94.54% of its initial specific capacity of 507 mAh g^{-1} after 600 cycles at a high current density of 5 A g^{-1}. This performance not only surpasses that of pristine NVO but also exceeds the majority of existing vanadium oxide cathode materials in terms of cyclic stability and capacity retention.

These findings underscore the potential of NVO-rGO composites in enhancing the practical applicability of AZIBs, suggesting a pathway to more sustainable, cost-effective, and safer battery technologies. The integration of theoretical insights and experimental validation in this research contributes to the field of energy storage, supporting the transition towards renewable energy sources by improving the efficiency and reliability of energy storage solutions.

Author Contributions: Conceptualization, H.L. and C.L.; methodology, H.L. and Y.Z.; software, Y.Z.; validation, H.L., C.L. and Y.Z.; formal analysis, H.L. and C.L.; investigation, H.L., C.L. and Y.Z.; resources, C.L.; data curation, Y.Z.; writing—original draft preparation, H.L.; writing—review and editing, H.L., C.L. and Y.Z.; visualization, C.L. and Y.Z.; supervision, H.L.; project administration, H.L.; funding acquisition, H.L. All authors have read and agreed to the published version of the manuscript.

Funding: This research was funded by the National Natural Science Foundation of China, grant number 22065032, and the Undergraduate Education and Teaching Research and Reform Project of Universities in Xinjiang Autonomous Region, grant number XJGXPTJG-202205. The APC was funded by High Level Overseas Educated Talents Returning to China Funding Candidate Program, grant number 2019160.

Data Availability Statement: The data presented in this study are available on request from the corresponding author.

Acknowledgments: The authors acknowledge the Shiyanjia Lab (www.shiyanjia.com accessed on 18 February 2024) for the TEM tests.

Conflicts of Interest: The authors declare no conflicts of interest.

References

1. Jia, X.; Liu, C.; Neale, Z.G.; Yang, J.; Cao, G. Active materials for aqueous zinc ion batteries: synthesis, crystal structure, morphology, and electrochemistry. *Chem. Rev.* **2020**, *120*, 7795–7866.
2. Wan, F.; Niu, Z. Design strategies for vanadium-based aqueous zinc-ion batteries. *Angew. Chem. Int. Edit.* **2019**, *131*, 16508–16517.
3. Chen, S.P.; Lv, D.; Chen, J.; Zhang, Y.H.; Shi, F.N. Review on defects and modification methods of $LiFePO_4$ cathode material for lithium-ion batteries. *Energy Fuels* **2022**, *36*, 1232–1251.
4. Jin, Y.; Zhang, T.; Zhang, M. Advances in intelligent regeneration of cathode materials for sustainable lithium-ion batteries. *Adv. Energy Mater.* **2022**, *12*, 2201526.
5. Zhang, Y.; Xu, J.; Liu, C.; Cheng, H.; Cai X.; Jia, D.; Lin, H. Ion-exchange-induced high-performance of inverse spinel Mg_2VO_4 for aqueous zinc-ion batteries. *J. Power Sources* **2022**, *549*, 232075.
6. Yimtrakarn, T.; Liao, Y.-C.; MV, A.S.; Chen, J.-L.; Chuang, Y.-C.; Lerkkasemsan, N.; Kaveevivitchai, W. Mn-Fe prussian blue analogue as low-cost robust cathode for non-aqueous Zn-ion batteries. *Mater. Today Commun.* **2023**, *34*, 105231.
7. Wu, B.; Zhang, G.; Yan, M.; Xiong, T.; He, P.; He, L.; Xu, X.; Mai, L. Graphene scroll-coated α-MnO_2 nanowires as high-performance cathode materials for aqueous Zn-ion battery. *Small* **2018**, *14*, 1703850.
8. Wang, J.; Liu, Z.; Wang, H.; Cui, F.; Zhu, G. Integrated pyrazine-based porous aromatic frameworks/carbon nanotube composite as cathode materials for aqueous zinc ion batteries. *Chem. Eng. J.* **2022**, *450*, 138051.
9. Guo, C.; Yi, S.; Si, R.; Xi, B.; An, X.; Liu, J.; Li, J.; Xiong, S. Advances on defect engineering of vanadium-based compounds for high-energy aqueous zinc-ion batteries. *Adv. Energy Mater.* **2022**, *12*, 2202039.
10. Ding, Y.; Zhang, L.; Wang, X.; Han, L.; Zhang, W.; Guo, C. Vanadium-based cathodes for aqueous zinc ion batteries: structure, mechanism and prospects. *Chin. Chem. Lett.* **2023**, *34*, 107399.
11. Zhang, N.; Wang, J.-C.; Guo, Y.-F.; Wang, P.-F.; Zhu, Y.-R.; Yi, T.-F. Insights on rational design and energy storage mechanism of Mn-based cathode materials towards high performance aqueous zinc-ion batteries. *Coord. Chem. Rev.* **2023**, *479*, 215009.
12. Chen, D.; Lu, M.; Cai, D.; Yang, H.; Han, W. Recent advances in energy storage mechanism of aqueous zinc-ion batteries. *J. Energy Chem.* **2021**, *54*, 712–726.

 doi:10.20944/preprints202405.0122.v2

13. Wang, X.; Zhang, Z.; Xi, B.; Chen, W.; Jia, Y.; Feng, J.; Xiong, S. Advances and perspectives of cathode storage chemistry in aqueous zinc-ion batteries. *ACS Nano* **2021**, *15*, 9244–9272.
14. Chen, D.; Lu, M.; Wang, B.; Cheng, H.; Yang, H.; Cai, D.; Han, W.; Fan, H.J. High-mass loading $V_3O_7{\cdot}H_2O$ nanoarray for Zn-ion battery: New synthesis and two-stage ion intercalation chemistry. *Nano Energy* **2021**, *83*, 105835.
15. Zhang, N.; Jia, M.; Dong, Y.; Wang, Y.; Xu, J.; Liu, Y.; Jiao, L.; Cheng, F. Hydrated layered vanadium oxide as a highly reversible cathode for rechargeable aqueous zinc batteries. *Adv. Funct. Mater.* **2019**, *29*, 1807331.
16. Zampardi, G.; Mantia, F.L. Prussian blue analogues as aqueous Zn-ion batteries electrodes: Current challenges and future perspectives. *Curr. Opin. Electrochem.* **2020**, *21*, 84–92.
17. Zhou, T.; Zhu, L.; Xie, L.; Han, Q.; Yang, X.; Chen, L.; Wang, G.; Cao, X. Cathode materials for aqueous zinc-ion batteries: A mini review. *J. Colloid. Interf. Sci.* **2022**, *605*, 828–850.
18. Zhou, J.; Shan, L.; Wu, Z.; Guo, X.; Fang, G.; Liang, S. Investigation of V_2O_5 as a low-cost rechargeable aqueous zinc ion battery cathode. *Chem. Commun.* **2018**, *54*, 4457–4460.
19. Chen, L.; Yue, H.; Zhang, Z.; Ma, Y.; Wang Y.; Xu, M.; Huang, Y.; Yuan, G. Pre-removing partial ammonium ions from the interlayer of ammonium vanadate with acid treating for quasi-solid-state flexible zinc ion batteries. *Chem. Eng. J.* **2023**, *455*, 140679.
20. Yin, B.; Zhang, S.; Ke, K.; Lee, W.S.V.; Wang, Z. Effects of small molecule interlayer engineering in vanadium oxide for zinc ion battery. *ChemistrySelect* **2020**, *5*, 8951–8958.
21. Tang, B.; Zhou, J.; Fang, G.; Liu, F.; Zhu, C.; Wang, C.; Pan, A.; Liang, S. Engineering the interplanar spacing of ammonium vanadates as a high-performance aqueous zinc-ion battery cathode. *J. Mater. Chem. A* **2019**, *7*, 940–945.
22. He, P.; Quan, Y.; Xu, X.; Yan, M.; Yang, W.; An, Q.; He, L.; Mai, L. High-performance aqueous zinc-ion battery based on layered $H_2V_3O_8$ nanowire cathode. *Small* **2017**, *13*, 1702551.
23. Li, K.; Liu, Y.; Wu, X. Ammonium vanadate electrode materials with stable layered structures for rechargeable zinc ion batteries. *CrystEngComm* **2022**, *24*, 5421–5427.
24. Xu, L.; Zhang, Y.; Zheng, J.; Jiang, H.; Hu, T.; Meng, C. Ammonium ion intercalated hydrated vanadium pentoxide for advanced aqueous rechargeable Zn-ion batteries. *Mater. Today Energy* **2020**, *18*, 100509.
25. Xu, J.; Zhang, Y.; Liu, C.; Cheng, H.; Cai, X.; Jia, D.; Lin, H. Al^{3+} introduction hydrated vanadium oxide induced high performance for aqueous zinc-ion batteries. *Small* **2022**, *18*, 2204180.
26. Tamilselvan, M.; Sreekanth, T.V.M.; Yoo, K.; Kim, J. Wide interlayer spacing ammonium vanadate $(NH_4)_{0.37}V_2O_5{\cdot}0.15(H_2O)$ cathode for rechargeable aqueous zinc-ion batteries. *J. Ind. Eng. Chem.* **2021**, *93*, 176–185.
27. He, D.; Sun, T.; Wang, Q.; Ma, T.; Zheng, S.; Tao, Z.; Jiang, J. Multi-functional potassium ion assists ammonium vanadium oxide cathode for high-performance aqueous zinc-ion batteries. *Batteries* **2022**, *8*, 84.
28. Qi, Y.; Huang, J.; Yan, L.; Cao, Y.; Xu, J.; Bin, D.; Liao, M.; Xia, Y. Towards high-performance aqueous zinc-ion battery via cesium ion intercalated vanadium oxide nanorods. *Chem. Eng. J.* **2022**, *442*, 136349.
29. Xu, L.; Zhang, Y.; Zheng, J.; Jiang, H.; Hu, T.; Meng, C. Ammonium ion intercalated hydrated vanadium pentoxide for advanced aqueous rechargeable Zn-ion batteries. *Mater. Today Energy* **2020**, *18*, 100509.
30. Wang, G.; Kuang, Q.; Jiang, P.; Fan, Q.; Dong, Y.; Zhao, Y. Integrating molybdenum into zinc vanadate enables $Zn_3V_2MoO_8$ as a high-capacity Zn-supplied cathode for Zn-metal free aqueous batteries. *Nanoscale* **2023**, *15*, 6722–6731.
31. Fan, L.; Li, Z. Highly stable cathode materials for aqueous Zn ion batteries: synergistic effect of pre-inserted bimetallic ions in vanadium oxide layer. *J. Alloy. Compd.* **2022**, *910*, 164872.
32. Cui, F.; Hu, F.; Yu, X.; Guan, C.; Song, G.; Zhu, K. In-situ tuning the NH_4^+ extraction in $(NH_4)_2V_4O_9$ nanosheets towards high performance aqueous zinc ion batteries. *J. Power Sources* **2021**, *492*, 229629.
33. Wang, W.; Liu, D.; Jiang, Y.; Zhang, D.; Shen, X.; Li, S.; Liang, J.; Xu, H. Mechanism enhancement of V_3O_7/V_6O_{13} heterostructures to achieve high-performance aqueous Zn-Ion batteries. *Chem. Eng. J.* **2023**, *463*, 142309.
34. Li, S.; Xu, X.; Wang, K.; Chen, W.; Lu, X.; Song, Z.; Hwang, J.Y.; Kim, J.; Bai, Y.; Liu, Y.; Xiong, S. Textured $Na_2V_6O_{16}{\cdot}3H_2O$ cathode tuned via crystal engineering endows aqueous Zn-ion batteries with high rate capability and adequate lifespan. *ACS Energy Lett.* **2022**, *7*, 3770–3779.
35. Wu, J.; Yang, Z.; Chen, H. Oxygen-deficient $HNaV_6O_{16}{\cdot}4H_2O$@reduced graphene oxide as a cathode for aqueous rechargeable zinc-ion batteries. *Ind. Eng. Chem. Res.* **2022**, *61*, 10640–10649.
36. Xu, L.; Zhang, Y.; Zheng, J.; Jiang, H.; Hu, T.; Meng, C. Ammonium ion intercalated hydrated vanadium pentoxide for advanced aqueous rechargeable Zn-ion batteries. *Mater. Today Energy* **2020**, *18*, 100509.
37. Tamilselvan, M.; Sreenkanth, T.V.M.; Yoo, K.; Kim, J. Wide interlayer spacing ammonium vanadate $(NH_4)_{0.37}V_2O_5.0.15(H_2O)$ cathode for rechargeable aqueous zinc-ion batteries. *J. Ind. Eng. Chem.* **2020**, *93*, 176–185.
38. Wu, Q.; Li, X.; Fan, H.; Cao, J.; Liu, X.; Wei, M.; Yang, L. Synergistic interlayer and structure engineering construction of layered hydrated vanadates/graphene for stable aqueous zinc-ion batteries. *J. Alloy. Compd.* **2023**, *941*, 168936.

 doi:10.20944/preprints202405.0122.v2

39. Yi, T.F.; Qiu, L.; Qu, J.P.; Liu, H.; Zhang, J.H.; Zhu, Y.R. Towards high-performance cathodes: design and energy storage mechanism of vanadium oxides-based materials for aqueous Zn-ion batteries. *Coordin. Chem. Rev.* **2021**, *446*, 214124.
40. Ren, H.Z.; Zhang, J.; Wang, B.; Luo, H.; Jin, F.; Zhang, T.R.; Ding, A.; Cong, B.W.; Wang, D.L. A V_2O_3@N–C cathode material for aqueous zinc-ion batteries with boosted zinc-ion storage performance. *Rare Metals* **2022**, *41*, 1605–1615.
41. Xing, Z.; Xu, G.; Xie, X.; Chen, M.; Lu, B.; Zhou, J.; Liang, S. Highly reversible zinc-ion battery enabled by suppressing vanadium dissolution through inorganic Zn^{2+} conductor electrolyte. *Nano Energy* **2021**, *90*, 106621.
42. Kresse, G.; Furthmüller, J. Efficient iterative schemes for ab initio total-energy calculations using a plane-wave basis set. *Phys. Rev. B* **1996**, *54*, 11169–11186.
43. Perdew, J.P.; Burke, K.; Ernzerhof, M. Generalized gradient approximation made simple. *Phys. Rev. Lett.* **1996**, *77*, 3865–3868.
44. Kresse, G.; Joubert, D. From ultrasoft pseudopotentials to the projector augmented-wave method. *Phys. Rev. B* **1999**, *59*, 1758–1775.
45. Blöchl, P.E. Projector augmented-wave method. *Phys. Rev. B* **1994**, *50*, 17953–17979.